Geophysical Prospecting
EAGE EUROPEAN ASSOCIATION OF GEOSCIENTISTS & ENGINEERS
Geophysical Prospecting, 2020, **68**, 1980–1998 doi: 10.1111/1365-2478.12937

Deep exploration using long-offset transient electromagnetics: interpretation of field data in time and frequency domain

Wiebke Mörbe[1]*, Pritam Yogeshwar[1], Bülent Tezkan[1] and Tilman Hanstein[2]

[1]*Institute of Geophysics and Meteorology, Department of Geoscience, University of Cologne, Cologne, Germany, and* [2]*KMS Technologies-KJT Enterprises, Inc., 11999 Katy Freeway, Suite 160, Houston, TX 77079, USA*

Received February 2019, revision accepted March 2020

ABSTRACT

In the framework of the Deep Electromagnetic Soundings for Mineral Exploration project, we conducted ground-based long-offset transient-electromagnetic measurements in a former mining area in eastern Thuringia, Germany. The large-scale survey resulted in an extensive dataset acquired with multiple high-power transmitters and a high number of electric and magnetic field receivers. The recorded data exhibit a high data quality over several decades of time and orders of magnitude. Although the obtained subsurface models indicate a strong multi-dimensional subsurface with variations in resistivity over three orders of magnitude, the electrical field step-on transients are well fitted using a conventional one-dimensional inversion. Due to superimposed induced polarization effects, the transient step-off data are not interpretable with conventional electromagnetic inversion. For further interpretation in one and two dimensions, a new approach to evaluate the long-offset transient-electromagnetic data in frequency domain is realized. We present a detailed workflow for data processing in both domains and give an overview of technical obstructions that can occur in one domain or the other. The derived one-dimensional inversion models of frequency-domain data show strong multi-dimensional effects and are well comparable with the conventional time domain inversion results. To adequately interpret the data, a 2.5D frequency-domain inversion using the open source algorithm MARE2DEM (Modeling with Adaptively Refined Elements for 2-D EM) is carried out. The inversion leads to a consistent subsurface model with shallow and deep conductive structures, which are confirmed by geology and additional geophysical surveys.

Key words: Data processing, Long-offset transient electromagnetics, Time/frequency domain.

1 INTRODUCTION

Since strategic important minerals often exhibit high electrical conductivities (e.g. Airo, 2015; Spagnoli *et al.*, 2016), electromagnetic methods are an important tool for mineral exploration. As the depth extension of existing mineral deposits is mostly unknown, methods are required to obtain deep information. In addition to a delineation of the depth of deposits, an understanding of the geological structures of the host rocks is essential. To combine a large penetration depth with a fast and dense area coverage, a semi-airborne method is developed within the Deep Electromagnetic Soundings for Mineral Exploration (DESMEX) project (Nittinger *et al.*, 2017; Schiffler *et al.*, 2017; Smirnova *et al.*, 2019), utilizing ground-based transmitters and airborne receivers.

Although no strategic important mineral deposits with geophysically well-detectable electrical conductivity characteristics are known in the surveyed area, massive highly conductive alum shales occur within the resistive host rock. The

*E-mail: moerbe@geo.uni-koeln.de

latter served as a reference target for the novel semi-airborne EM exploration concept. Additional land-based long-offset time-domain EM measurements were carried out to provide a validation model for the semi-airborne concept.

Land-based controlled source electromagnetic methods (CSEM) exhibit a high-resolution as well as a high-penetration depth and are therefore an important tool to gain insights to deep geological formations. The utilized long-offset transient electromagnetic method is an active electromagnetic method that uses a galvanically coupled electrical dipole as a source. Typically, a square wave source function is transmitted. By measuring the transient response of the electric and magnetic field components at offsets up to several times the target depth, the method is typically applied to retrieve information about deep structures. The depth of investigation reaches several km (e.g. Ziolkowski *et al.*, 2007; Haroon *et al.*, 2015). Overviews of the long-offset transient-electromagnetic (LOTEM) method regarding its theory and practical applications can be found in, for example Kaufman and Keller (1983) and Strack (1992). LOTEM data are traditionally interpreted in time and not in frequency domain. Advantages of time-domain CSEM methods over frequency-domain methods have been shown by a few authors (e.g. Strack, 1992; Zhdanov, 2010). One major advantage is that the transient response of the Earth can be measured in the absence of the primary field (Streich, 2016).

For the presented dataset, a time-domain interpretation imposes various difficulties. First, the measured EM response in the survey area is superimposed by an induced polarization (IP) response, which hinders a conventional EM inversion of the late time step-off response. Second, the survey area is located in a rather complex geological setting and cannot be interpreted via a one-dimensional (1D) approach. Although multi-dimensional time-domain modelling algorithms have been presented by, for example Martin (2009), Commer (2003) and Oldenburg *et al.* (2012), open source inversion tools for time-domain land-based CSEM are still not commonly available and not routinely utilized. In contrast, for frequency-domain evaluation, a range of multi-dimensional open source codes (Key and Ovall, 2011; Grayver *et al.*, 2013) is available. Furthermore, the computational requirements of frequency-domain codes are typically lower.

In this study, we analyse whether the measured LOTEM data can be interpreted in both domains without a significant loss of information and in the presence of IP. Furthermore, we discuss under which circumstances interpretation in one domain is beneficial. First, we introduce a workflow for the processing of the data in both domains and illuminate the technical demands for each method. The dataset is introduced, and the relative responses in both domains are evaluated, showing subsequently a comparison of time and frequency inversion results in 1D. Finally, we present a 2.5D inversion of the data in frequency domain, including a geological description of the shallow subsurface structures as verification.

2 LOTEM VALIDATION STUDY: SURVEY AREA AND SET-UP

As a validation area for the Deep Electromagnetic Soundings for Mineral Exploration (DESMEX) semi-airborne exploration concept, a former antimony mining area located in the Thuringian Slate mountains was selected. The area is part of the Berga anticline, consisting out of several shale and quartzite units from Ordovician age, partly covered by thin layers of Silurian to Middle Devonian black shales (Dill, 1993). The regional geological strike direction follows the dominant Variscian strike from north-east to south-west. Due to the local restriction of antimony to lenticular sectioned ore bodies ranging from several decimetres to maximum 4 m (Liebe *et al.*, 1912; Gräbe *et al.*, 1996) and a resistivity greater than 100 Ωm of antimony ore (Airo, 2015), the antimony mineralization itself cannot be resolved with electromagnetic methods. Based on geophysical investigations (Steuer *et al.*, 2015) and geological outcrop maps (Fig. 1), the occurrence of Silurian alum (graptolite) shales and middle Devonian black shales is well known. The shales exhibit resistivitites below 10 Ωm, leading to a large electrical conductivity contrast compared to that of the host material, with a few hundred Ωm. Therefore, it is a suitable target for demonstrating the newly developed semi-airborne EM concept. Consequently, the presented long-offset transient-electromagnetic (LOTEM) study aims to reach a maximum exploration depth and a high data coverage to provide an optimal validation model. However, the area is in a heavily faulted geological setting and thus highly complex. Furthermore, the presence of graptolite shales can produce anisotropy and induced polarization effects. Usually, complementary information from geology and petrophysics is mandatory for a full geophysical interpretation of the electrical subsurface image.

An extensive survey was carried out in summer 2016 and 2017 (Fig. 1a). In total, 6 transmitter positions in broadside configuration (along the regional geological strike direction) as well as 52 E-field receiver stations along an 8.5 km long profile were set up. A schematic sketch of the survey layout for one exemplary transmitter site is given in Fig. 1(b). Transmitter amplitudes between 10 and 24 A and a transmitter length of ∼1 km could be realized. Using multiple transmitter

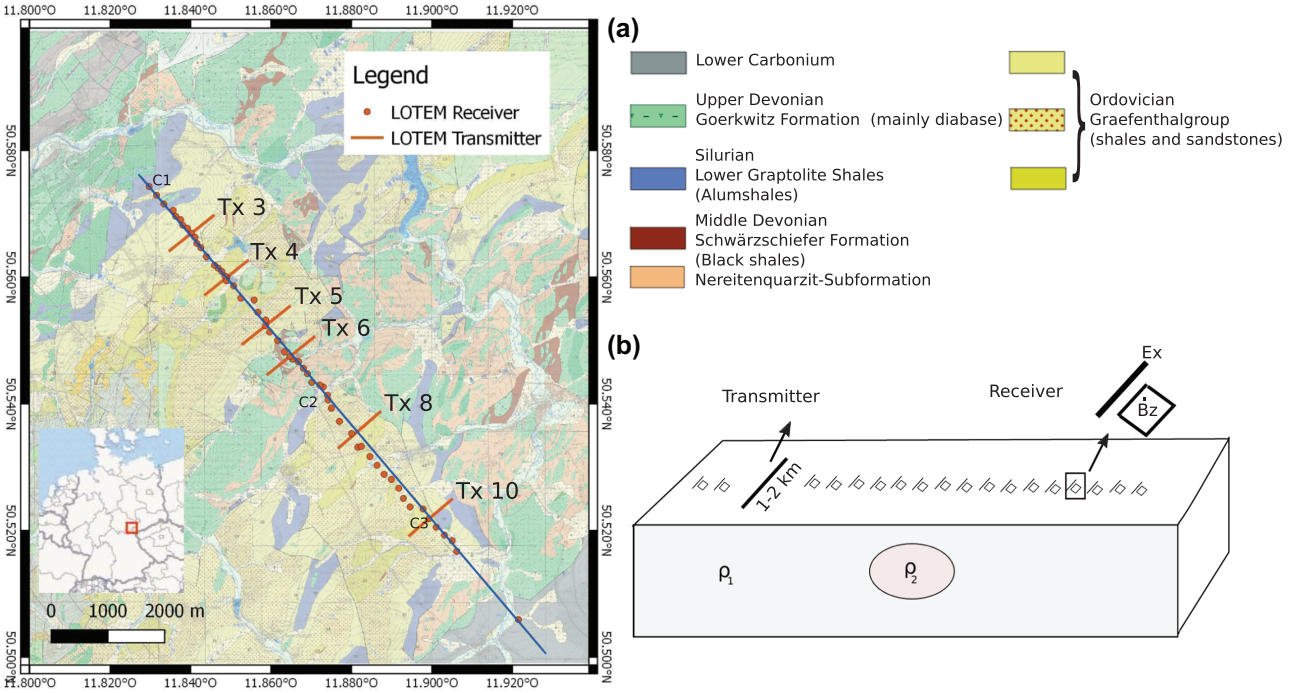

Figure 1 (a) Location of the LOTEM transmitters and receivers deployed during the field campaign 2016 and 2017 along a 10 km long profile (blue transect) on top of a digital geological map (Liebe *et al.*, 1912; Gräbe *et al.*, 1996) of Thuringia (Germany). The direction of the profile is perpendicular to the geological strike direction of the area. C1–C3 denote the locations of conductive alum shale. In total, 52 receiver stations using multiple sources were deployed, focusing on the E-field component parallel to the transmitter. (b) Schematic sketch of a typical broadside layout for a single transmitter-receiver configuration as used in the validation study. For each transmitter stations, the E-field component within an offset range of 500 m up to 4 km was measured. Additionally, for some stations, the time derivative of the vertical magnetic field was recorded.

locations for most of the receiver stations, in total, 170 Ex-field datasets (parallel to transmitter/strike direction) with dipole lengths between 40 and 60 m were measured.

Considering the available geological information about the survey area, the switching time of the transmitter, the sampling rate of the data logger and the chosen offsets between transmitter and receiver stations were defined by modelling studies beforehand (Mörbe, 2020), aiming to resolve a conductive target in depth greater than 1 km. Using a sampling frequency of 50 kHz and a switching time of up to 1 second, transients with a time range over four decades could be recorded. An accurate time synchronization between transmitter and receiver sites was ensured by GPS synchronization utilizing a pulse per second signal, where the trigger points were selected to be in phase with a common reference time.

We used a high-power and fast-switching Zonge GGT 30 transmitter. A rectangular signal with switching times between 450 and 1050 ms was injected. As the signal was overall more stable and exhibited a shorter ramp, a 50% duty cycle was preferred over a 100% duty cycle.

A relatively short ramp time of ~120 microseconds for a step-off procedure for a dipole length of 1000 m enables data acquisition also in the early times. The step-on signal exhibits more distortions produced by the transmitting device and usually has a longer ramp time. The spectrum (Fig. 2b) of the utilized transmitter function exhibits sharp peaks for the odd harmonics of the base frequency.

At the receiver stations and for current recording, we used KMS-820 acquisition units from KMS Technologies and SPAM Mk 4 devices from the Geophysical Instrument Pool Potsdam. Depending on the offset, the local noise level and the utilized switching time, data were recorded between 30 min and up to 2 h at each receiver station in order to improve the signal to noise ratio, running up to eight stations simultaneously. Subsequently, the measuring equipment was moved to the next receiver site.

3 DATA PROCESSING

Analysis of the data in frequency and time domains is possible depending on the capabilities of the used instrumentation.

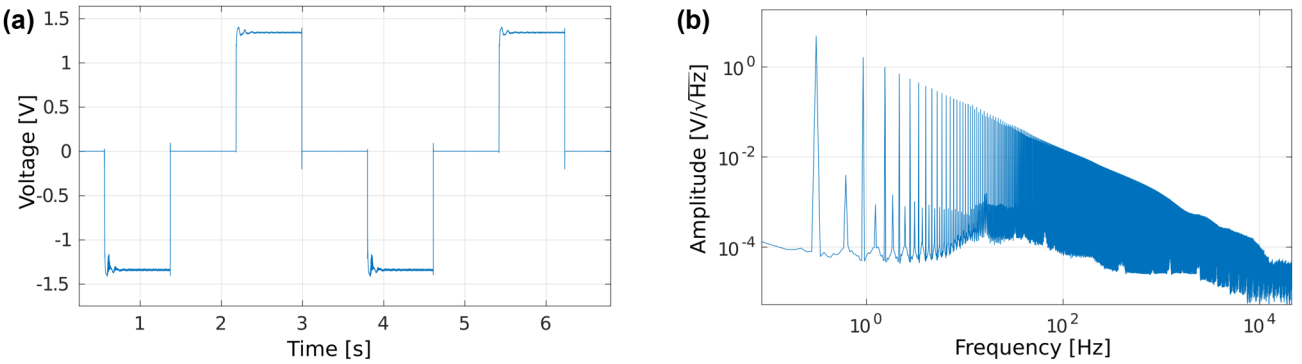

Figure 2 (a) Utilized transmitter signal measured by a current clamp, 50% duty cycle and (b) spectrum of the raw current data. A switching time of 810 ms (period of 3.24 seconds) was used in this example. The peaks visible in the spectrum correspond to the base frequency of 0.3086 Hz and its harmonics.

Time domain measurements have usually higher requirements on the utilized transmitters and receivers. One of the most critical points for time-domain applications is the creation of a fast and clean switching ramp function. A sharp ramp signal is not crucial in the frequency domain since the full waveform is analysed. However, if the transmitter is capable of performing a fast switch off/on of the current, the signal amplitude of high frequencies is larger. This property might be beneficial for interpretation of the shallow subsurface, since high-order odd harmonics can be evaluated. In time domain, sharp voltage gradients, for example produced by a fast current time off in highly resistive environments, often lead to oscillations. Therefore, whether the loggers are capable of an undisturbed time series recording in time domain must be evaluated beforehand. For frequency-domain processing, the full current waveform must be recorded continuously. In time domain, only a short record of the early-time transmitter current is needed in order to calculate the system response. However, since shifts or amplitude drops in the time series can occur, it is advisable to observe the transmitted current over the complete measurement duration in both domains. Having equipment capable of transient EM measurements, it is from a technical point of view possible to process and interpret the dataset in both domains.

Since the measurements were performed in a heavily industrialized area with several anthropogenic noise sources (pipelines, railways and powerlines), coherent noise can bias the recorded long-offset transient-electromagnetic (LOTEM) data. To improve the signal to noise ratio, several processing steps are required to obtain a high-quality transient in time domain or a transfer function in frequency domain for each station. To pick the correct onset of the transient (time domain) or have a synchronous recorded receiver signal and transmitter signal (frequency domain), accurate time synchronization between the receiver and transmitter is required. Therefore, the transmitter is triggered by a GPS clock and is synchronized with the GPS data of the data loggers. To simplify the processing routine and prevent errors, the trigger point was set to be in phase with a common reference time (i.e. 06.00.00 AM UTC-time).

3.1 Time-domain processing workflow

In the survey area, several anthropogenic noise sources are present. To increase the signal-to-noise ratio by minimizing the ambient noise present in the data, transient measurements at one location are stacked between 1000 and 5000 times. By selecting appropriate switching times beforehand, the periodic reoccurrence of the most dominant noise sources can be utilized to minimize its influence during the stacking procedure. Considering a 50% duty cycle and as main noise contributions 50 Hz (20 ms), 150 Hz (6.67 ms) and 16.7 Hz (60 ms), half a signal period ($T/2$) must fulfil the criterion

$$\frac{T}{2} = n\ 60\ \text{ms}. \tag{1}$$

n stands for any integer number. (n element N)

Hence, after half a period, the noise is in phase. Considering the negative sign of the signal in the second half of the period, which will be multiplied by a factor of -1 during processing, the periodic noise contributions can be effectively reduced during stacking. Considering the prior known resistivity distribution in the survey area as well as the estimated depth of investigations, switching times of, for example 450 or 810 ms, that is, periods of 1.8 or 3.24 seconds, resulted in a sufficiently long transient length and reduced the main noise

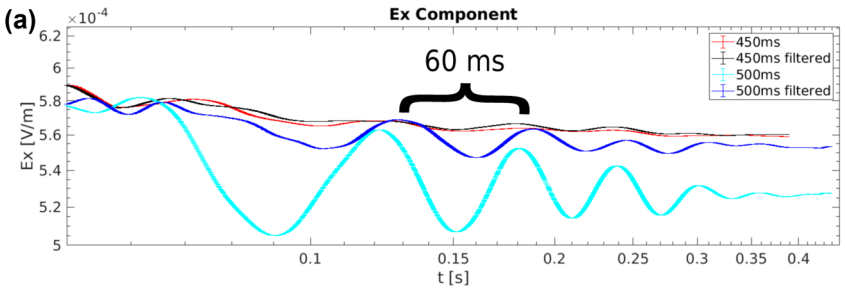

(b)

T_{switch}	50 Hz	16.7 Hz
450 ms	✓	✓
500 ms	✓	X
810 ms	✓	✓
1000 ms	✓	X
1050 ms	✓	✓

Figure 3 (a) The difference in bias due to railway noise using two switching times. For all transients, the same smoothing coefficients and number of stacks were used. (b) Overview of switching times suitable for noise reduction by stacking. For the LOTEM validation study, switching times of 450, 810 and 1050 ms were used.

contribution during the stacking procedure. Note that for a 50% duty cycle, one period contains four current switches.

In Fig. 3(a), the advantages of an appropriate transient length to minimize the periodic noise contribution in the observed electrical field data are demonstrated. Without applying additional filter techniques during the processing of the data, the difference is remarkable. In the stacked data, the railway noise of 60 ms is clearly visible in the 500 ms long transient, whereas it is markedly reduced in the 450 ms long transient. Even after applying a digital three-point filter, the 500 ms signal still contains periodic noise contributions. Hence, the 450 ms switching time is clearly superior in terms of noise suppression compared with the 500 ms switching time. Figure 3(b) lists the suitability of exemplarily selected switching times regarding the property of periodic noise suppression by stacking.

Depending on the cable length of the dipole transmitter and the maximum current amplitude employed, the ramp time of the transmitter during the survey ranged from 100 to 150 microseconds (Fig. 4). In this time range, oscillations in the transmitter ramp can be observed. To interpret the early times (<120 microseconds) correctly, a system response must be recorded at the transmitter site in addition to the recorded signal at the receiver sites. The measured field response $y(t)$ can be expressed as a convolution (denoted by "$*$") between the system response $s(t)$ and the unaffected Earth response $x(t)$ (Strack, 1992):

$$y(t) = s(t) * x(t). \tag{2}$$

The transmitter ramp, the utilized sensors and recording system will influence the measured signal. For the E-fields, a LEM current clamp (Life Energy Motion, LEM Europe GmbH) was used to record the transmitted current, assuming that the influence of the used receiver electrodes can be neglected, and therefore, only the transmitter ramp function needs to be considered. For the time derivatives of the magnetic field, the system response depends on both, the transmitter waveform and the characteristics of the utilized

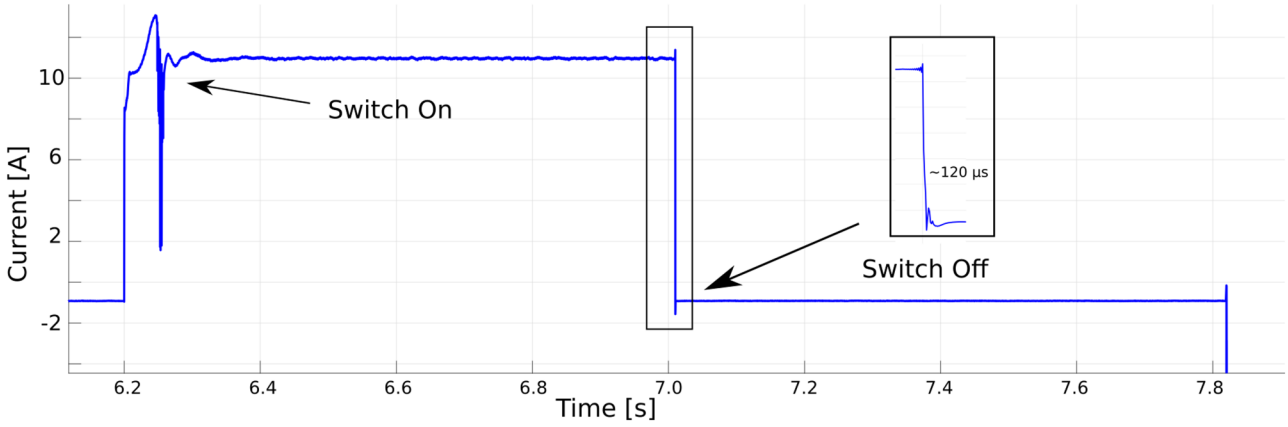

Figure 4 Transmitted step-on and step-off signals. The step-on signal shows distortions over a broad time range. The ramp time of the step-off signal is 120 microseconds.

induction coil. Therefore, the system response was measured in field at stations close to the transmitter. Here we assume, that the influence of the earth response is negligible for short offsets and early times, which are the most affected by the system response (Scholl, 2001). Since the step-on signal was heavily distorted and showed an influence of the ramp time of up to ~0.1 second (Fig. 4), it was not used for further interpretation, and only step-off signals were considered.

Figure 5 shows the processing steps applied in the time and frequency domains for the example of one electric field recording taken at a distance of 630 m from the transmitter. For time-domain processing, after the definition of the time-zero of the transient at the start of the current switch off via GPS synchronization, the steps illustrated in Fig. 5(a–d) are applied:

- To average out the highest ratios of correlated EM noise, a three-point filter (similar to, e.g. Kingman *et al.*, 2004; Pankratov and Geraskin, 2010) is applied to the dataset, which exploits the periodicity of the transmitting signal in half periods. Each point in the time series is averaged with the point half a transmitting period later. At the end of the time series, the filter moves backward in time, applying the averaging scheme in the opposite direction. Figure 5(a) shows the effect of the three-point filter. Noise components are reduced, the linear drift is removed, and the mean value of the time series is shifted to zero.
- We then apply a selective stacking method including error estimation (Hanstein *et al.*, 1986). Each filtered time series is cut into the number of current switches that it contains. To utilize the maximum number of data available, negative transients are multiplied by a sign factor. However, the late times in particular are still affected by correlated high-frequency noise. Subsequently, a smoothing scheme, averaging the data over a continuously increasing interval with a variable Hanning window weighting function (Hanstein *et al.*, 1986), is applied to the stacked dataset. Figure 5(b) shows the improved stacked and smoothed step-off transient on a log–log scale. As clearly seen, high-frequency noise is removed from the data.
- After filtering, stacking, cutting and smoothing of the data, the transient is normalized to the receiver dipole length or coil area. To reduce the number of data points for efficient inversion, the transient is interpolated to 10 logarithmic equidistant time points per decade (Fig. 5c).
- Figure 5(d) shows the system response recorded at the transmitter with a current clamp; it was normalized to its area, and the time derivative was taken to obtain the impulse response of the system. Recording with a current clamp directly provides a system response for electric field measurements (provided the response of the clamp itself is negligible). For magnetic fields, the responses of the field sensors need to be included to obtain the full system response. Since a deconvolution with the noise-affected measured field data can lead to numerical instabilities, a stable convolution of the system response with forward-modelled data is applied during the inversion process (Hördt, 1989).

The step-off signal was levelled to the late time DC response of the previous step-on prior to further interpretation. Having a high signal-to-noise ratio for the overlying DC level, the errors for the electrical field component tend to be less than 1%. For offsets up to 4 km for most stations, high-quality E-field transients with transient lengths of up to 1 second could be obtained.

3.2 Frequency-domain processing workflow

For frequency-domain interpretation of the LOTEM dataset, the raw time series was transformed and processed in frequency domain (Fig. 5e–h). We used a robust magnetotelluric processing scheme based on Egbert and Booker (1986) and adapted the evaluation frequencies to the odd harmonics of the transmitter signal. For frequency-domain processing, additional to the recorded time series, a full record of the transmitted signal must be obtained.

- To reduce the effect of the periodic noise contribution, we defined Fourier coefficients ranging between ±1 Hz of the base frequency of the noise (e.g. 50 Hz and harmonics), which were excluded from further processing. To illustrate the bandwidth of the noise signal, Fig. 5(e) shows an example power spectrum ranging from 448 to 452 Hz of a 10 min long section of the recorded time series. Having 450 Hz as an odd harmonic of the 50 Hz powerline noise, the peak in the power spectrum at this frequency can be identified as an unwanted noise frequency. Varying along 449–451 Hz over the 10 min recording time, frequencies of 450 ± 1 Hz were defined as affected by noise and excluded from further processing.
- We then Fourier transform the data (Fig. 5f). In the raw data, the base frequency and its odd harmonics as well as the harmonic noise frequencies of the powerline and the railway are clearly visible. In the reduced spectrum, excluding frequencies defined in the previous step, the powerline and railway noises are removed. For the next steps, only the base frequencies of the switching period and its odd harmonics (marked with black circles) up to the

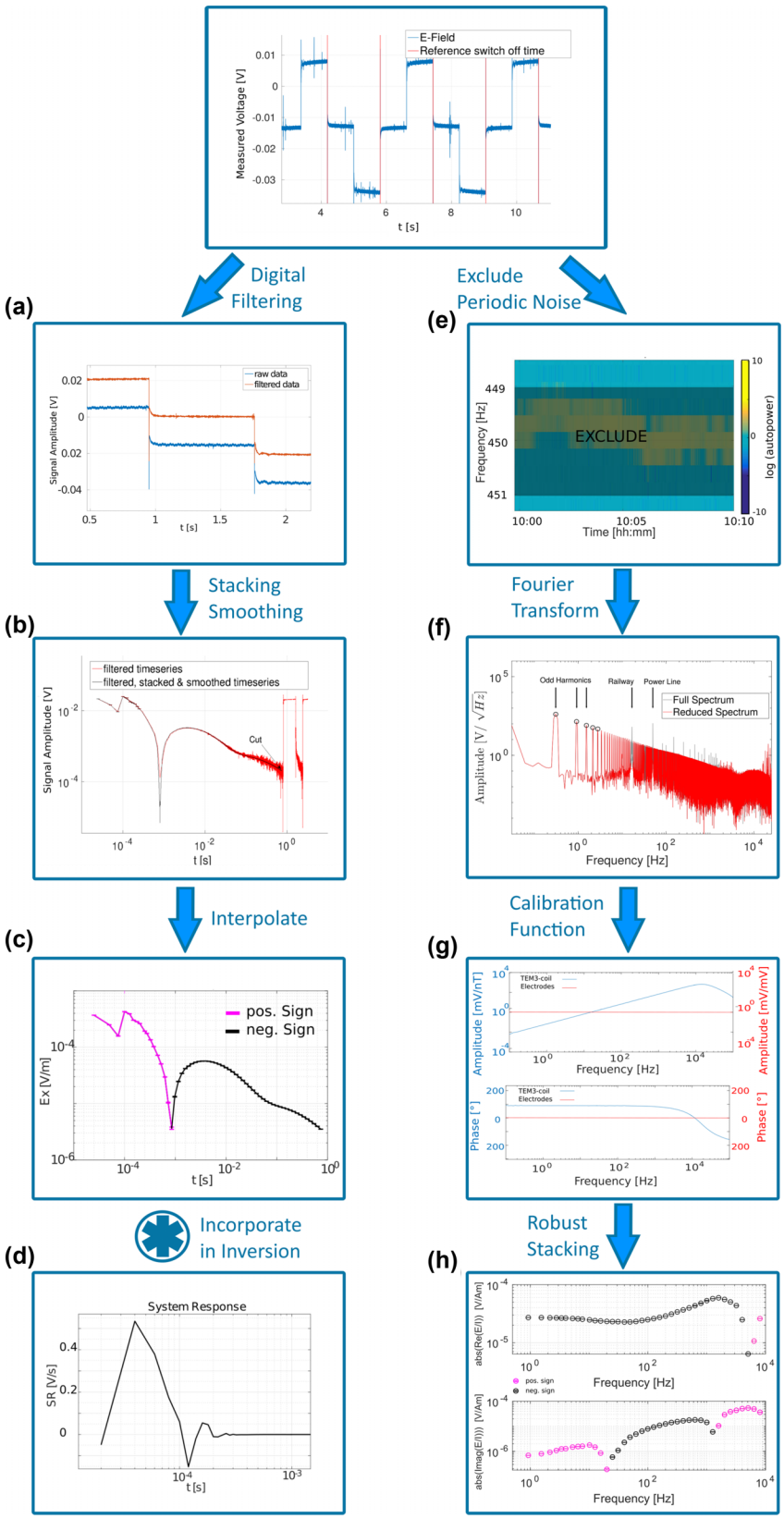

Figure 5 Processing steps from raw data to post-processed data for an exemplary E-field station. Left side: steps carried out for time-domain evaluation. Starting from the raw time series, the transient is filtered, cut and smoothed. Additionally, the system response is calculated. Right side: processing steps carried out for frequency-domain evaluation. The raw data are transformed into frequency domain, and the transfer function between the measured field response and transmitted current is calculated. If frequency-dependent system responses are present, a calibration function is multiplied.

Nyquist frequency at 20 kHz are evaluated. This procedure is applied to both time series, the transmitter signal and the receiver signal, analogously.

- To cope with the frequency dependence of the used sensors, a calibration function must be multiplied with the spectrum after the Fourier transformation, as shown exemplarily in Fig. 5(g) for the induction coil (TEM-3 by Zonge Engineering) used to record the magnetic field at that station. The non-polarizable electrodes used for the E-field recording are assumed to be frequency independent; therefore, the signal must be only normalized by the dipole length of the receiver.
- To calculate the transfer function between transmitted and received signals, the recorded and preprocessed spectrum is normalized by the current function. After the application of a robust stacking routine, the Fourier coefficients are averaged in 10 logarithmically distributed frequencies per decade for consistency with the time-domain transients (Fig. 5h).

The calculated transfer functions exhibit a high data quality over all frequencies up to ∼1 kHz for all offsets. For offsets smaller than 1 km, reliable transfer functions up to 10 kHz (limited by the sampling frequency) could be obtained. Errors calculated using the robust stacking procedure tended to be smaller than 1% for frequencies up to 10 kHz, except at sign reversals. We reduced the frequency range for inversion since we utilized different data loggers to record the current at the transmitter and the field components at the receiver, which exhibit a different internal delay. We corrected for that, but small time shifts (∼10 microseconds) are possible due to the limited sampling rate and therefore limited resolution in time, which would affect the data at high frequencies. Additionally, correlated high-frequency noise as visible in the full spectrum of the time series (compare Fig. 5f) might affect the high-frequency content. Those frequencies can be interpreted when appropriate errors for high-frequency noise and possible time shifts are applied. Since the focus on the LOTEM study is to achieve a deep subsurface model, frequencies above 1 kHz are excluded in the following comparison and inversion.

3.3 Comparison of time- and frequency-domain data

After processing a high-quality dataset was obtained in both domains. Figure 6 shows the post-processed normalized voltages measured for the electric field in time- and frequency domain for Tx8 exemplarily. Since the time-domain data are subsequently inverted as step-on transients ($\mathbf{E}_{on}$), the post-processed step-off transients ($\mathbf{E}_{off}$) were subtracted from the DC field ($\mathbf{E}_{DC}$) approached in the late time step-on response by taking (Kaufman and Keller, 1983)

$$\mathbf{E}_{on} = \mathbf{E}_{DC} - \mathbf{E}_{off}. \tag{3}$$

The acquired standard errors from the processing are small in both domains. For most of the stations, only the step-off data for late times and the imaginary part of the frequency-domain transfer function around sign reversals and high frequencies exhibit errors >1 %. Since in the step-on depiction of the data, the DC level is overprinting the inductive parts of the signal, the voltages are higher than those in the step-off depiction. For the same reason, the dynamic range of the step-off transients is higher, reflecting the inductive signal decreasing over time. For late times, the step-on data tend to the static DC level, whereas the step-off data reflect the decrease in the inductive signal to low voltages. As expected, close to the source, located at profile metre 5880, and at early times, the measured voltages are the highest, and they decrease with increasing offset to the source. Note that the decrease in the measured voltages is asymmetric for step-on data, with higher values in the south-east and lower values in the north-west of the transmitter. This observation is an indication of a 2D distribution of electrical conductivity in the subsurface, suggesting higher resistivities in the south-eastern part of the profile.

A similar behaviour can be observed in the post-processed transfer functions displayed as real and imaginary parts along the profile. The real part reflects a combination of the primary field and the inductive signal similar to the step-on content of the data. The imaginary part of the transfer function, which is not overprinted by a galvanic term, exhibits a higher dynamic range and decreases to zero, when the field response reaches the DC level. Sign reversals are present in the step-off representation of the dataset as well as in the frequency-domain data.

Under consideration of a relative error floor, which takes geometrical errors into account, an inversion of the step-off time-domain dataset would be beneficial. For step-off transients, the inductive signal is at late times not overprinted by the DC signal, which can be up to two to four decades higher. Therefore, inclusion of the DC level in the inversion decreases the influence of the inductive part of the signal significantly. Late time inductive information in particular is lost, leading to a possible decrease in resolution. When jointly interpreting data from both real and imaginary parts, the inductive information is decoupled from the primary field in the imaginary part.

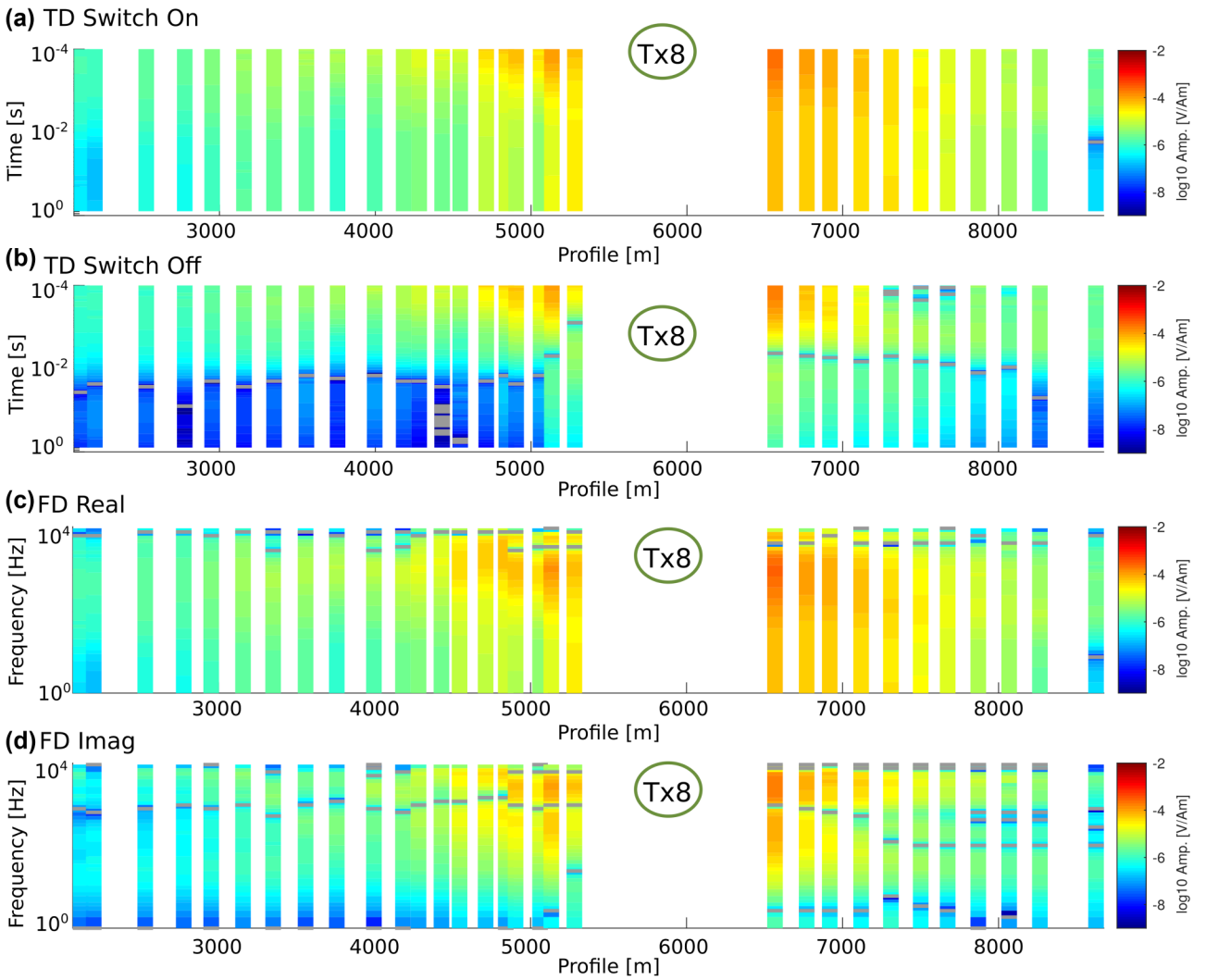

Figure 6 Post-processed electrical field data for transmitter Tx8 displayed for (a) time-domain switch-on transients, (b) time-domain switch-off transients, (c) the real part of the frequency-domain transfer function, and (d) the imaginary part of the frequency-domain transfer function. Voltages are plotted under the corresponding receiver station. The dataset is normalized to the current and receiver length. Grey markers indicate the locations of sign reversals.

4 COMPARISON OF ONE-DIMENSIONAL INVERSION RESULTS IN TIME AND FREQUENCY DOMAIN

To verify to what extent an interpretation of the long-offset transient-electromagnetic (LOTEM) data in time and frequency domains delivers similar information about subsurface structure, we compare one-dimensional (1D) smooth Occam inversion (Constable *et al.*, 1987) models calculated for both domains. In time domain, we focus on electric field step-on transients, being less influenced by induced polarization (IP) effects, as shown in Section 4.1. As the starting model, a 30-layer case with logarithmically increasing layer thicknesses and resistivities of 300 Ωm is used. Transfer functions are inverted using a frequency range between the base frequency, ranging between 0.24 and 1 Hz, and odd harmonics up to 1 kHz. Frequencies greater than 1 kHz were excluded prior to inversion. For time-domain data, accordingly a time range for transients starting from 10^{-3-3} seconds up to 1 second was used. The statistical data errors derived from processing were small for both domains. To cope with static, systematic and geometrical errors and geologic noise (Spies and Frischknecht, 1991) that are not taken into account in the processing error, an error floor of 1% was applied to time-domain data and

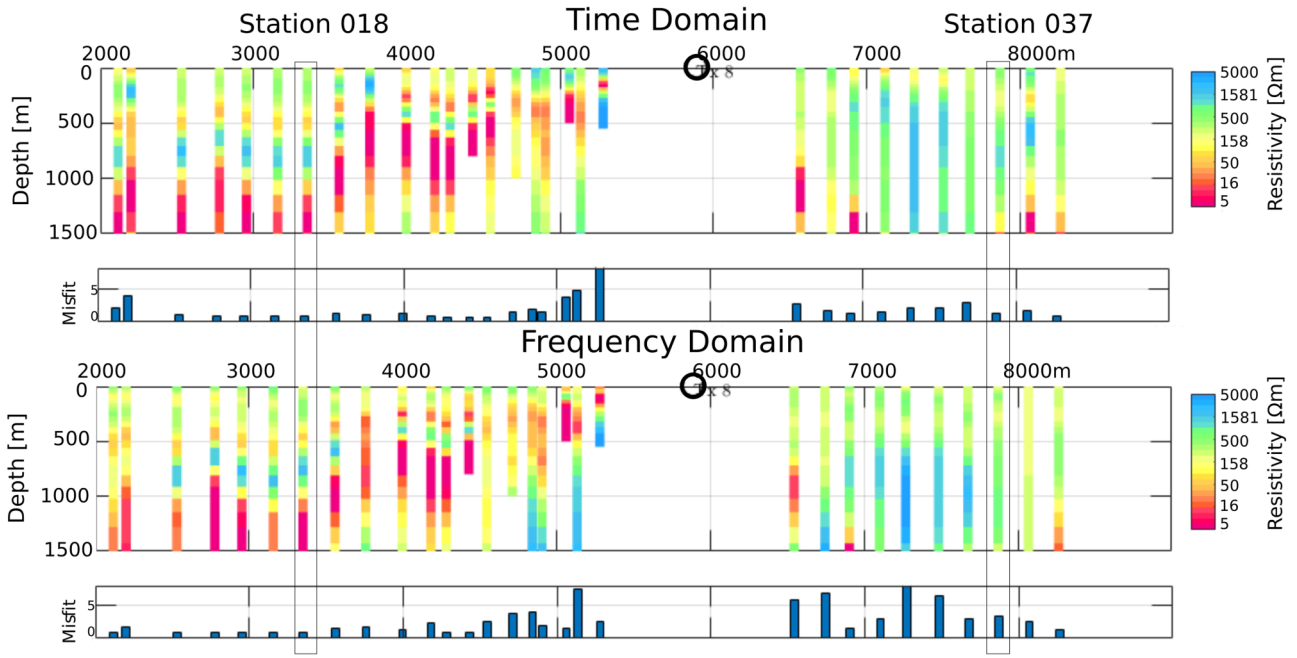

Figure 7 Results of 1D time-domain inversion and 1D frequency-domain inversion utilizing an Occam R1 approach illustrated in colour code. The inversion results for transmitter location Tx8 (black circle) are plotted under the corresponding receiver position. Below the inversion models, the averaged weighted data misfit is plotted for the corresponding dataset. Two exemplary stations shown in Figs. 8 and 9 are labelled and marked with a grey box.

3% to frequency-domain data. In addition, the errors for data points around sign reversals were increased to 100%. Since the frequency-domain transfer functions exhibit a higher dynamic range and convergence problems, a higher relative error floor was set in frequency domain in order to stabilize the inversion.

The resulting Occam R1 inversion models are plotted exemplarily for Tx8 in Fig. 7 at the location of the corresponding receiver station. A comparison of Occam inversion models using the first-order (R1) and second-order (R2) derivatives of the smoothness constraints (Constable *et al.*, 1987) gives an approximate guess of the depth of investigation. For regions where both obtained models show similar structures, the corresponding model parameters are well resolved. If the inversion results from Occam R1 and Occam R2 diverge, the inversion result is dominated by the regularization constraint and cannot be trusted (e.g. Cai *et al.*, 2018; Yogeshwar *et al.*, 2020). The length of the plotted model columns is determined using the abovementioned criteria. For most stations, inversion models of both, Occam R1 and Occam R2 are similar within 2 km depth. The error (e_i)-weighted root-mean-square (RMS), here defined as

$$\chi = \sqrt{\frac{1}{N}\sum_{i=1}^{N}\frac{(d_i - \mathbf{F}_i(\mathbf{m}))^2}{e_i^2}} \qquad (4)$$

between the forward-modelled data $\mathbf{F}_i(\mathbf{m})$ and the observed data $\mathbf{d}_i$ summed and normalized over $\mathbf{N}$ data points is plotted below the Occam inversion models.

The averaged weighted data fit (equation (4)) of the LOTEM 1D inversion is 2.0, and the overall misfit of the frequency-domain data exhibits a higher value of 2.7. For the frequency-domain models, the overall misfit of the more resistive part of the profile in the SE is higher than that in the more structured part in the north-west. Note that in both methods, the effects of IP are not included, which can bias the inversion results to a different degree in both domains. For most of the stations, the Occam inversion results of both methods are comparable. In both inversion profiles, the most prominent structure is a resistive layer on top of a more conductive structure in depth ranges of ~1000 m between profile metres 2000 and 3500, increasing up to 500 m at profile metre 4500. Figure 8 shows the Occam R1 and R2 models and the corresponding Occam R1 data fit for a station in the north-west part of the profile and Fig. 9 one station exemplarily for the more resistive part of the profile located in the south-east. All four models for both stations yield similar results over the displayed depth range down to 2500 m. The observed data and model fit of the Occam R1 inversion for the frequency-domain transfer function and the time-domain

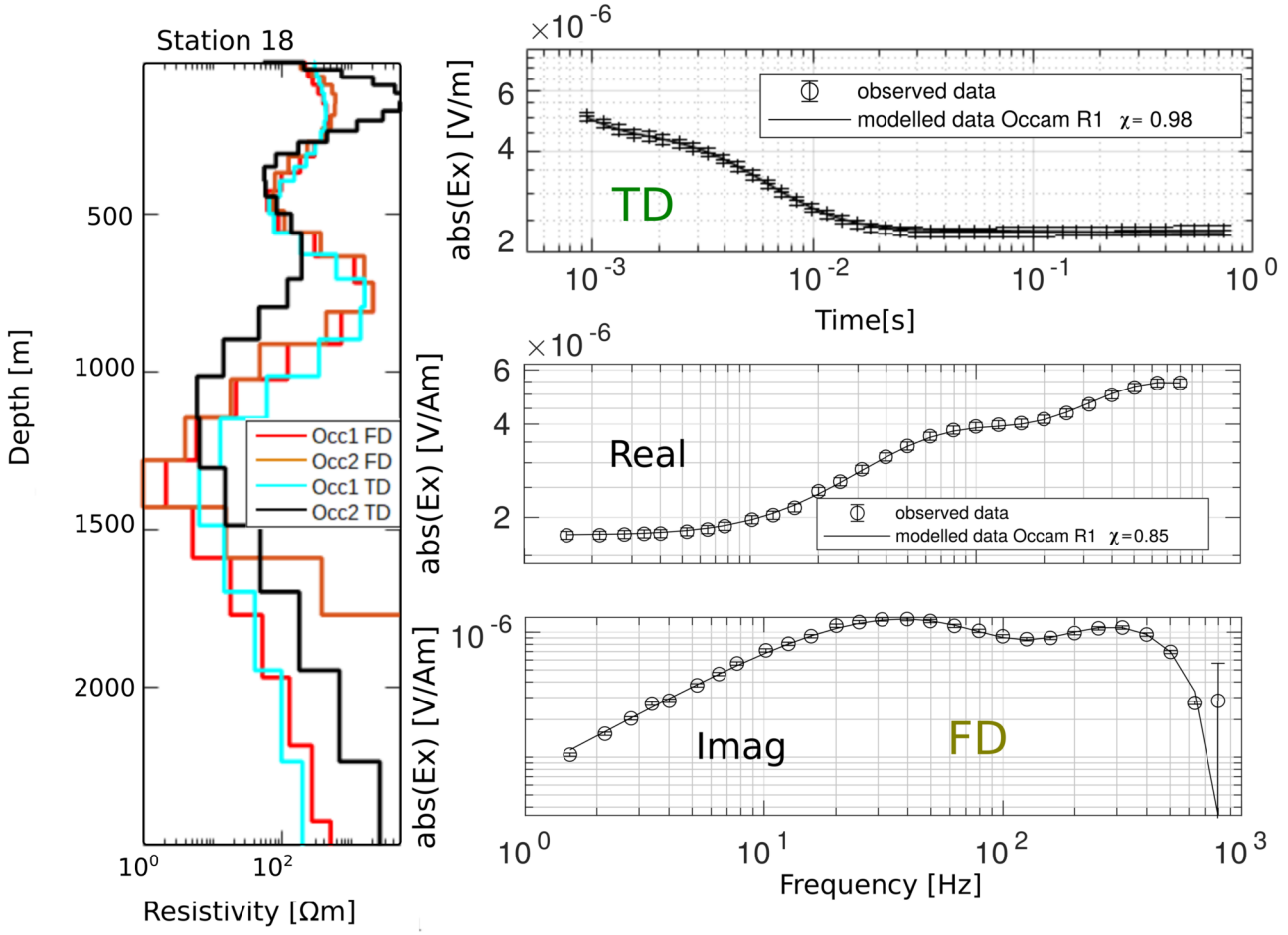

Figure 8 The Occam R1 and Occam R2 results for the time-domain and frequency-domain inversion and the data fit for station 18.

transient demonstrate that both datasets are well explained by the model for stations 18 and 37. The behaviour of the Occam R1 and Occam R2 models suggests a depth of investigation of ~1500 m for station 18 and 2500 m for station 37.

The stitched view of the 1D inversion results already exhibit a strongly 2D subsurface in terms of resistivity. To adequately interpret the data, a multi-dimensional inversion of the dataset must be carried out.

4.1 1D resolution analysis in both domains

To analyse the resolution of the model parameters in 1D, a singular value decomposition was carried out, and the set of eigenparameters (EPs) were calculated for a synthetic three-layer case for frequency-domain data and time-domain step-on data. The model was extracted from a simplified subsurface model derived from station 18. The synthetic model was preferred over the real inversion model to ensure comparability for the inversion statistics. Synthetic transfer functions were calculated between 1 Hz and 1 kHz, that is, transients from 10^{-3} to 1 second, respectively.

A more detailed description of the SVD method can be found in, for example Zhdanov (2002). The result of the EP analysis is displayed following Scholl and Edwards (2007), where the relative weights of the logarithm of the original parameters contained in each EP are displayed as circles (Fig. 10). The radius of each circle represents the magnitude of each contribution to the EP. The colour of the circle represents positive and negative values. Following Edwards (1997), the standard error in an EP is the reciprocal of its eigenvalue. Values of the standard error are displayed along the x-axis and refer to the relevance of the EP. Scholl and Edwards (2007) considered EPs with reciprocals of their eigenvalues greater than 0.067 as not resolvable. Δ_{max} expresses the fractional errors of the logarithmic model parameters and gives an estimate of whether the original model parameter is resolved. As an

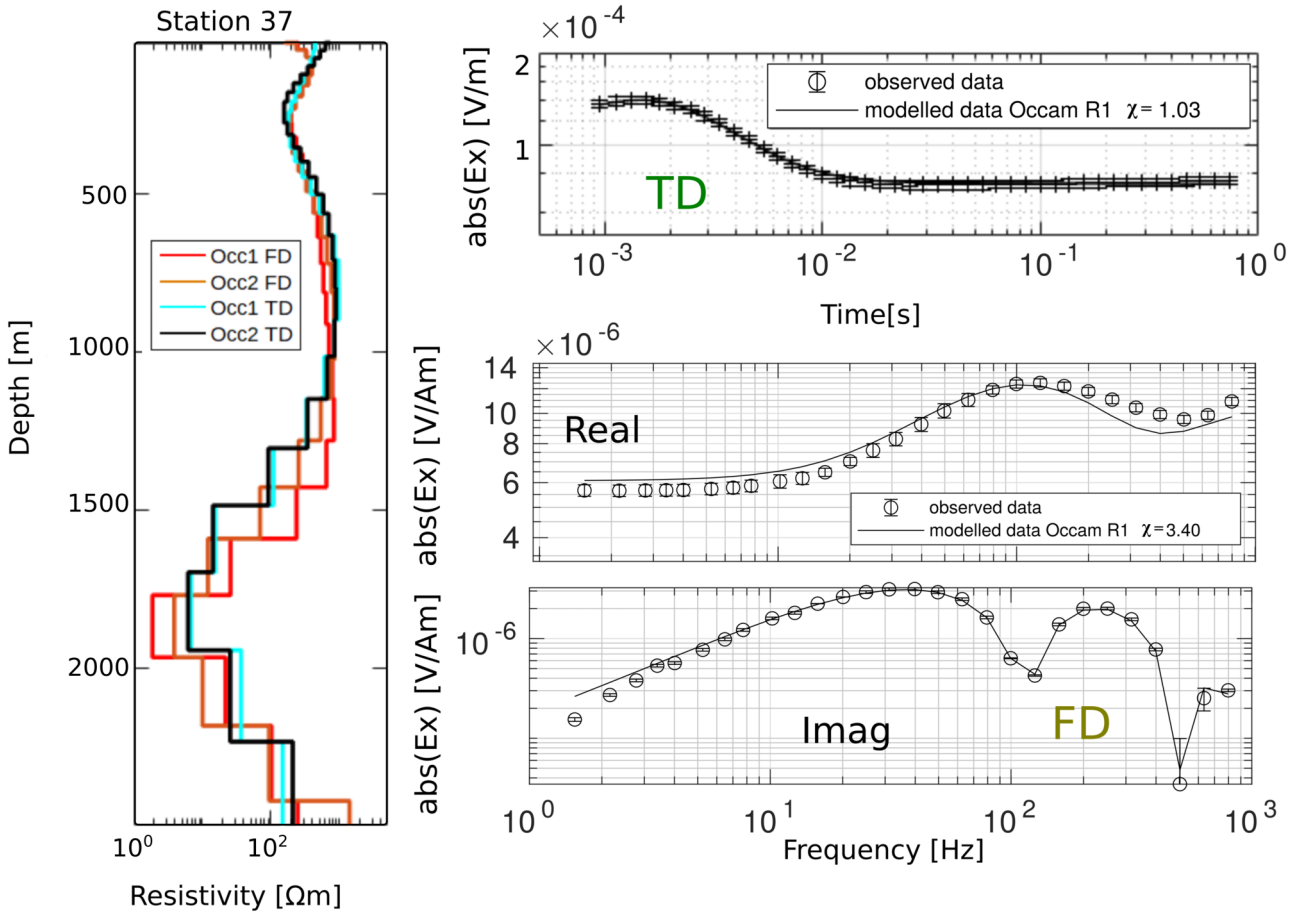

Figure 9 The Occam R1 and Occam R2 results for the time-domain and frequency-domain inversion and the data fit for station 37.

additional measure of the resolution of a model parameter, the back-transformed singular values (BTSVs) can be calculated (Hördt, 1992); these contain the eigenvalues of the EP, related as

$$\mathbf{Q} = \sqrt{\mathbf{Ve}(\mathbf{Ve})^T}, \tag{5}$$

where **e** corresponds to the normalized eigenvalues of the parameter space eigenvector matrix **V**. It therefore contains values between 0 and 1. The highest value exhibits the best resolution of the corresponding model parameter.

To obtain a direct comparison of the error-weighted SVD parameters, a relative error floor of 1% was set for both time-domain data and frequency-domain data for modelling the SVD parameters prior to inversion. In addition, an absolute error floor obtained from field measurements was set for both domains.

Looking at the distributions of the model parameters relative to the eigenvalues, both domains exhibit a similar behaviour. Having the thickness d_1 as the dominant contributor to the most relevant EP with low upper error bounds, this model parameter is the best resolved parameter in frequency and time domains, as also indicated by the highest BTSV. Both methods are able to resolve the resistivity and thickness of the first two layers. The last layer exhibits a considerably higher Δ_{max} as well as a higher error for the EP most influenced by it and is therefore less resolved than the other parameters. Note that the absolute values of the BTSV between different models (i.e. domains) cannot be compared directly to each other since the values are normalized to the highest calculated value. However, one can observe that the influence of the first layer on the modelled dataset is higher in frequency domain than in time domain. Nevertheless, all layers exhibit a smaller Δ_{max} in frequency domain compared to the time domain. Therefore, all parameters are better resolved in the frequency domain when considering an equivalent relative error floor of 1% for both datasets. Note that the assigned error floor scales directly with the fractional errors of the model parameters. When relative error floors utilized for the inversion of field data are

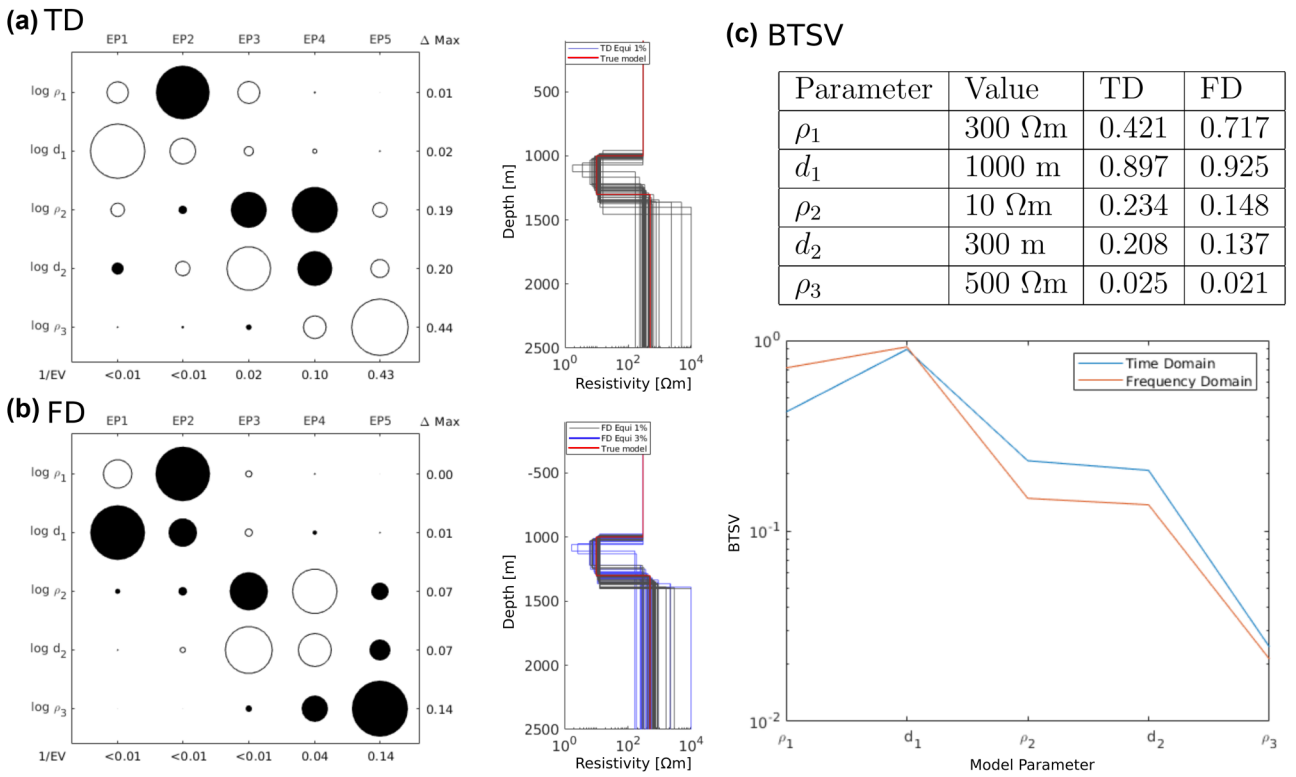

Parameter	Value	TD	FD
ρ_1	300 Ωm	0.421	0.717
d_1	1000 m	0.897	0.925
ρ_2	10 Ωm	0.234	0.148
d_2	300 m	0.208	0.137
ρ_3	500 Ωm	0.025	0.021

Figure 10 (a) Eigenvalue analysis for time-domain data and (b) frequency-domain data obtained by the inversion of forward-modelled data from the true model assuming an error floor of 1% for both domains. Next to the eigenvalues, we display the synthetic model and equivalence models as obtained via inversion. For the frequency domain, equivalence models were calculated for both a 1% error floor (grey) and 3% error floor (blue), as utilized in the inversion of the field data. (c) Synthetic model and calculated BTSV for each model parameter.

considered (1% for TD and 3% for FD data), the errors of the model parameters are in similar ranges in both domains. Next to the EP and the BTSV, the synthetic model and the equivalence models that exhibit a χ less than 1 of the best fit Marquardt model are plotted. Again, the first two layers are well constrained by the Marquardt model since the equivalence models show only a small deviation from the model parameters of the best fit model, whereas the resistivity of the last layer is poorly defined in both domains. For the second and third layers, the variations in the equivalence models are smaller in frequency domain if a relative error of 1% is considered. If the relative error is increased to 3%, more equivalence models that fit the data within the given error bounds are found. The resolution of the second and third layers in time and frequency domains assuming a 1% error for the first and a 3% error for the latter is comparable. One reason for the better resolution of the frequency-domain data compared with the time-domain step-on data considering the same relative errors is the joint inversion of real part and imaginary part compared with an inversion of only step-on transients in the time domain. Although both time-domain step-on data and frequency-domain real-part data are overprinted by the DC level, the imaginary part exhibits a higher relative inductive response. Note that this difference in resolution is not physical but rather due to the non-equivalent ratios between the inductive response and primary field and is therefore dependent on the relative error settings. Note that the advantage in resolution disappears if step-off data can be evaluated; these data exhibit a purely inductive response in the near field of the transmitter (Kaufman and Keller, 1983).

The study of the EP and BTSV analysis for this simplified synthetic three layer model leads to two conclusions: first, the SVDs for both domains exhibit a similar weighting of the model parameters to the corresponding EP. Second, taking the error levels of the real field dataset into account, no loss of resolution for deep targets is expected when inverting the LOTEM dataset in the frequency instead of time domain. Both thickness and resistivity of the upper two layers are well resolved by the frequency- and time-domain inversions of the E-field LOTEM data.

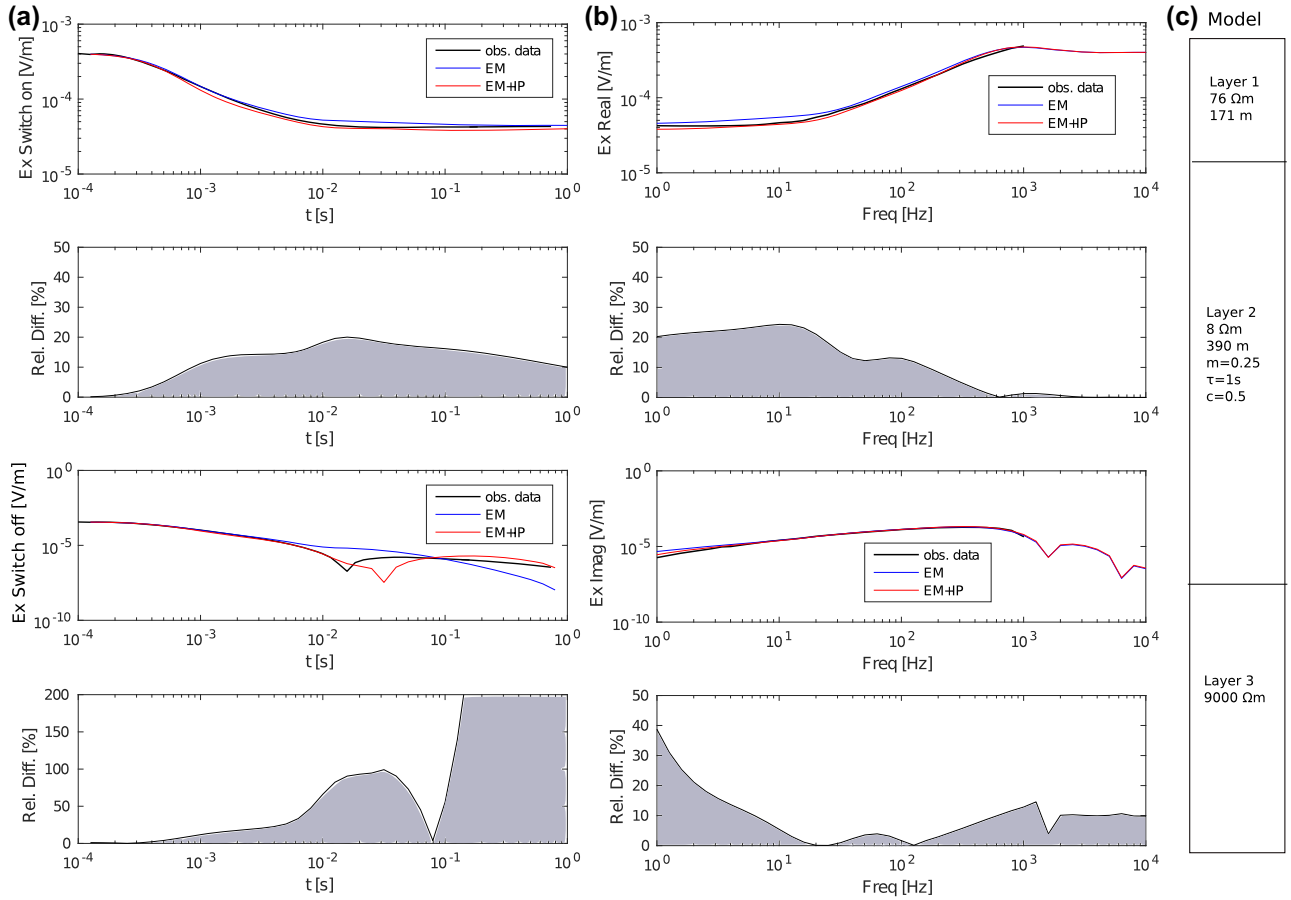

Figure 11 (a) Comparison of the model response in time domain without IP parameters (blue) and with IP parameters (red). The model is based on the Marquardt inversion of data from station with an offset of 1000 m to Tx8. The observed data from the station are plotted in black. Data are shown with DC level (step-on) and without DC level (step-off). Additionally, the relative difference between the model response with and without IP parameters is displayed. (b) Modelled data in the frequency domain and relative difference for the same model used in (a). For the EM forward calculation, the chargeabilities were set to 0 for all layers. The utilized model parameters are listed in (c).

4.2 The influence of induced polarization in both domains

Martin *et al.* (2018) conducted shallow dipole–dipole time domain induced polarsation (TDIP) measurements in the survey area to characterize the geometry and properties of the conductive graptolite shales. The measurements revealed strong polarization effects with chargeabilities on the order of 250 mV/V in the survey area, which the authors related to the presence of graptolite shales. For broadside electrical field data, as measured in the presented LOTEM dataset, the IP response exhibits the opposite sign to the inductive response (Nabighian and Elliot, 1976; Hoheisel *et al.*, 2004). Therefore, especially for late times, where the inductive effect decayed to small values and the IP effect is increasingly strong, the transient response is dominated by the latter, and sign reversals in the step-off transients can occur. For step-on data, where the inductive response is overprinted by the DC level, the IP response will lead to a decrease in the measured amplitude. Figure 11 illustrates effects of induced polarization on step-off and step-on data as well as the real and imaginary parts in time and frequency domains for one given receiver–transmitter offset. A station at a distance of 1000 m to the transmitter site was selected as an exemplary station in order to interpret only a small induction volume, and therefore, relatively small 2D effects in the dataset can be assumed. The 1D forward study was performed using an IP + EM forward-modelling algorithm (Hoheisel, 2000), where next to the modelling of EM transients, IP parameters for each layer can be included. The depth and resistivity of the EM forward model given in Fig. 11(c) are based on a Marquardt 1D inversion (Levenberg, 1944; Marquardt, 1963) obtained by inverting step-on data only. For modelling of the IP parameters, the Cole–Cole model

(Cole and Cole, 1941) is utilized, where the induced polarization is expressed in terms of the chargeability m, relaxation time τ and dispersion coefficient **c**. The IP parameters were set to values based on the findings of Martin *et al.* (2018).

Here, the conductive layer was assumed to be responsible for IP effects. Therefore, IP parameters were assigned to this layer only, and the EM + IP responses in time and frequency domains (Fig. 11a and b) were modelled. Additionally, the measured data for the given receiver–transmitter offset are displayed.

Note that the presence of IP and an integration of IP effects in the inversion process would influence the layer thickness and conductivity of the inversion result and is therefore probably not the best fitting model for the given dataset. However, with the modelling study, the relative influence of the induced polarization on step-on and step-off data in the time domain and on real and imaginary data in the frequency domain can be compared. The relative difference between the forward-modelled EM response and the EM + IP response is plotted for each case over time and frequency, respectively. In the time domain, the IP response is most dominant for late times. As expected, the relative misfit and therefore the relative influence of the IP response is up to an order of magnitude larger for step-off data than for step-on data. In the real part of the frequency-domain data, the IP effects are equivalent to the late times in the time domain, the highest for long periods. The relative influence of IP is larger in the imaginary part, where the IP response is distributed over a wide frequency band. Nevertheless, the relative difference between the IP model response and the EM model response is smaller than for the step-off data. The real part is similar to the step-on response overprinted by the DC level and therefore exhibits a small relative difference between the two modelled transfer functions.

This modelling study considering those strong IP parameters shows that late time step-off data cannot be successfully inverted by an EM inversion algorithm. The influence on step-on data and frequency-domain data is less significant. When interpreting the dataset neglecting IP effects, only either early-time information of step-off data and step-on data using large error floors or frequency-domain data can be inverted. Note that for cases in which the IP response is the target parameter, one should invert time-domain step-off data with a joint inversion of IP and EM parameters since the relative IP response is the largest in step-off transients. Since here, the data are interpreted considering the EM response only, the step-off data could not be interpreted.

5 2D INVERSION IN FREQUENCY DOMAIN

For further interpretation of the frequency-domain dataset, a 2.5D inversion was conducted using the finite element open source EM code MARE2DEM (Key and Ovall, 2011). The resulting inversion model is displayed in Fig. 12(a). Frequencies between 1 and 1000 Hz were included in the inversion. We inverted the dataset transformed as amplitude and phase since it showed an improved convergence behaviour compared with inversion of the real and imaginary parts. To speed up the inversion process, frequencies and corresponding amplitudes measured for different base frequencies were interpolated to one common array containing 10 values per decade. An error floor of 5% was assigned to the amplitude and a constant error floor of 2° to the phase, which exhibited improved convergence during inversion and was therefore slightly up-weighted. In total, 7140 data points from 52 E-Field stations utilizing all six transmitter positions were included. As the starting model, a homogeneous half space of 300 Ωm was used. For modelling of the dipole, a dipole approximation for the transmitters was applied, and the topography was considered.

The inversion result after 20 iterations is shown with a weighted RMS of 3.7. The misfit is higher compared to the one-dimensional (1D) inversion results, for which each inversion is completely decoupled from neighbouring soundings, often leading to better data fitting. Deviations from a fit within the error bounds are most likely due to induced polarization and 3D effects, which can bias some parts of the dataset. However, considering the high quantity of data included in the inversion, a robust geophysical 2D model of the survey area could be obtained. The averaged misfit for amplitude and phase along the profile for all six transmitter positions is plotted below the inversion model (Fig. 12b). Data from stations exhibiting strong outliers were removed prior to inversion, and global bounds of the resistivities were fixed to values between 1 and 10,000 Ωm. Observed data and modelled data for two stations from transmitter Tx8 are displayed in Fig. 12(c). It can be observed that phase values for high frequencies are rather poorly fitted, which is a general tendency for the dataset along the profile. The overall misfit over frequency for both exemplary stations is reasonable. The average misfit is higher in the central part of the profile, with a maximum at approximately $x = 6$ km. The grey lines represent isolines of the summed-up, to the cell-size normalized and error-weighted sensitivities of amplitude and phase of 10^3 and 10^4. Those values correspond to the 71th and 87th percentile, respectively. The absolute value of sensitivity does not give insights into the resolution of a structure. However, the

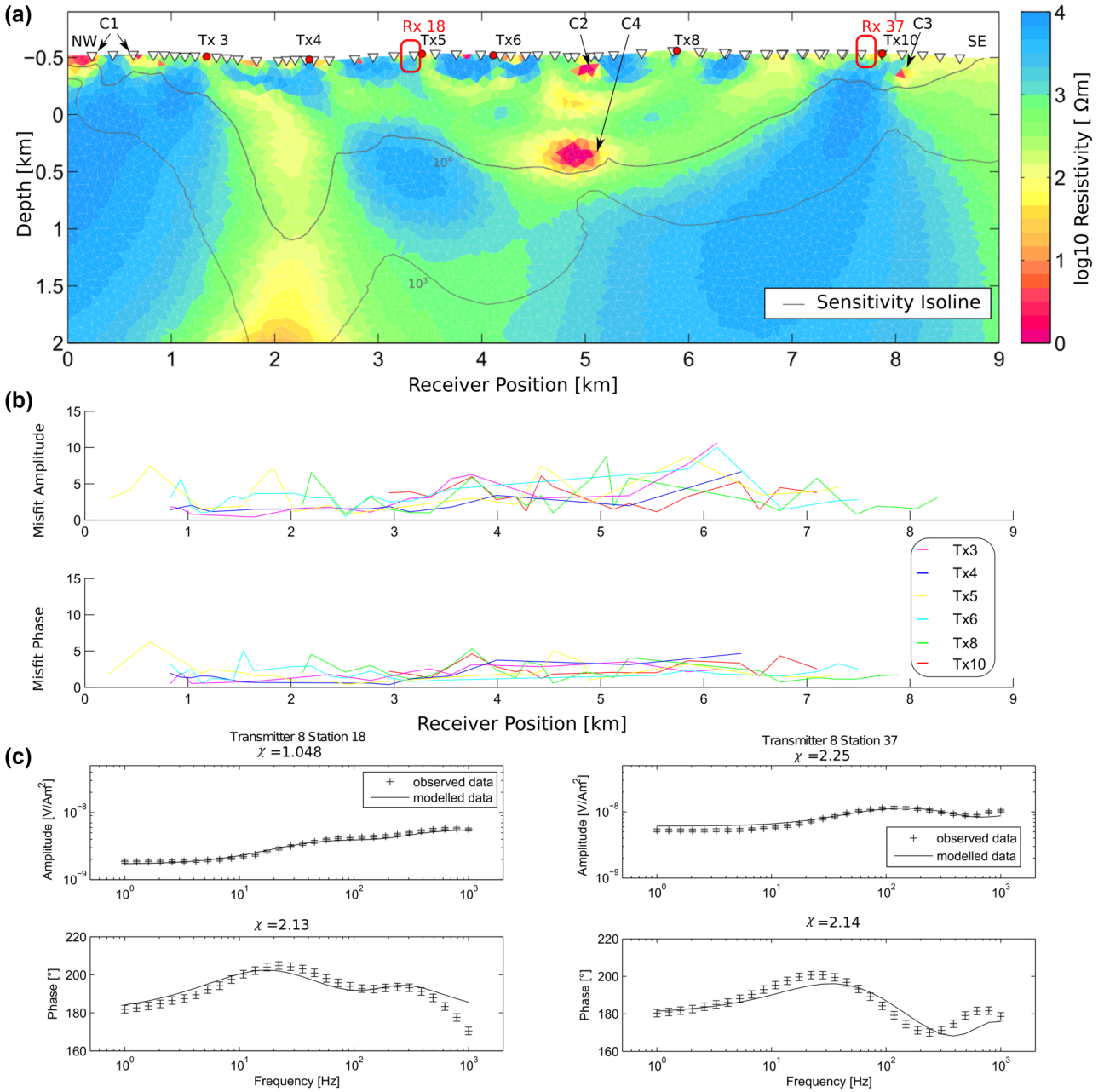

Figure 12 2.5D inversion of electric field data using the open source CSEM inversion code MARE2DEM. (a) Obtained 2D conductivity model. After 20 iterations, the RMS is reduced from 11.25 to 3.7. (b) Error-weighted misfit along the profile for phase and amplitude. (c) Observed data and model response for two exemplary stations marked in red and utilizing transmitter location Tx8. The four local high conductive structures are marked as C1, C2, C3 and C4.

isolines of sensitivities give insight into the relative resolution of subsurface structures throughout the model, reflecting the conductivity distribution of the subsurface and utilized survey geometries. The sensitivity in the south-eastern part of the profile is low due to a relatively sparse station distribution and high resistivities in the area. The conductive structure C4 in the middle of the profile is well resolved in return. The structure dipping to the south-east suggested by the 1D inversion of the dataset of the transmitter Tx8 (Fig. 7) is not present in the 2D inversion but is probably caused by the anomaly C4 and C2 with its response stretched downwards for larger offsets.

However, for a full geological interpretation of the deeper subsurface and the geological structures causing the EM response and the subsequent inversion model displayed in Fig. 12, all geophysical and geological information must be combined in an integrative subsurface model and interpreted jointly since the geology in the area is rather complex. The study of induced polarization (IP) effects was not the aim of this work; therefore, the frequency data were inverted, where the effect of IP is still present and can bias the inversion result to a certain degree, but exhibiting a smaller relative response. For other applications, where the IP parameter can deliver valuable information about the targets, for example in mineral exploration, inversion of step-off long-offset transient-electromagnetic (LOTEM) data in the time domain including the EM response and IP parameters should be performed. Nevertheless, the shallow conductive structures C1–C3 correspond well with the location of the conductive graptolite shales in the outcrop map (Fig. 1). The anomalies C1 and C3 exhibit a smaller extension and are covered by less data, however sensitivity in both regions is high. All shallow anomalies can also be found in the inversion results of the semi-airborne (Smirnova *et al.*, 2019) and HEM (Steuer *et al.*, 2015) methods. The 2D inversion of the LOTEM data evaluated in the frequency domain leads to a consistent subsurface model, confirming that the frequency-domain interpretation of the dataset is a suitable approach.

6 CONCLUSIONS

To validate a novel semi-airborne controlled source electromagnetic methods (CSEM) exploration concept for deep mineral exploration, a large-scale long-offset transient-electromagnetic (LOTEM) field survey was conducted in a former mining area in Schleiz, Germany. In total, six high-power transmitters and 52 E-field sensors were deployed along a 8.5 km long profile. We adopted different processing workflows to evaluate the LOTEM data in both time and frequency domains. The processing scheme results in high-quality transfer functions for time-domain step-on and step-off as well as frequency-domain real and imaginary electric field data.

Due to source over-print from the primary field, the real part of the frequency domain as well as the step-on response provide lower resolution in terms of the inductive information content. A rather simple modelling study qualitatively explained sign reversals in the step-off transient data, which were produced by strong induced polarization (IP) effects occurring from graptolite shale. On the one hand, step-off response data are beneficial because IP effects can be identified better than in step-on or FD data representations. On the other hand, conventional one-dimensional (1D) EM interpretation is not possible with step-off data, which are superimposed by IP. Step-on and frequency-domain transfer functions can be interpreted using a 1D EM approach and result in very comparable conductivity models. The resolution is high towards deep conductive structures, and the inversion statistics in both domains exhibit very similar parameter resolution in terms of back-transformed singular values (BTSV). We could clearly validate that our processing and inversion scheme for the evaluation of LOTEM data is adequate in both domains and provides sufficient depth resolution.

All three data representations indicate clearly multi-dimensional subsurface features due to an asymmetric data characteristic with respect to the transmitter, leading to incorrect 1D stitched inversion models with obvious multi-dimensional features. The derived 2.5D inversion for all transmitters and receivers in the frequency domain provides a consistent and meaningful model. Shallow and deep conductive structures correlate well with complementary geophysical results and geological background information. The derived 2 model has high sensitivities up to a depth of 1–1.5 km.

From our analysis, we obtain three major conclusions: (1) Equipment and survey settings typically used for time domain applications are commonly also suitable for subsequent frequency-domain evaluation. If the utilized instrumentation is capable of both time- and frequency-domain data acquisition, it is clearly advisable to adjust the surveying parameters accordingly. (2) The relative target responses in the data representations differ, even if the information content of the dataset is not changed by Fourier transformation. Therefore, evaluation in one domain or the other or even both domains can be beneficial and should be considered. For example, if high relative errors due to, for example set-up errors overprint the inductive response in the time-domain step-on response, an evaluation in the frequency domain is beneficial. In particular, IP affects both domains and step-off as well as step-on data differently on a relative scale, which can be helpful in the interpretation. (3) The possibility to evaluate data in both time and frequency domains results in a larger choice of available multi-dimensional inversion routines.

ACKNOWLEDGEMENTS

We would like to thank the field team of the DESMEX Survey 2016 and 2017 and the DESMEX work group. Furthermore, we would like to thank the Geophysical Instrument Pool Potsdam (GIPP) for provision of the SPAM Mk IV System and

support (grant numbers 201608 and 201716). In addition, we thank Michael Becken for provision of the magnetotelluric processing scheme EMTS and a 1D frequency-domain inversion code. DESMEX is funded by the Federal Ministry of Education and Research (BMBF) under BMBF grant 033R130. We thank the editor and the reviewers for their suggestions, which helped us to significantly improve the manuscript.

ORCID

Wiebke Mörbe https://orcid.org/0000-0002-3959-6951

REFERENCES

Airo, M.-L. (2015) Geophysical signatures of mineral deposit types in finland. *Geological Survey of Finland, Special Paper*, 58, 9–70.

Cai, J., Tezkan, B. and Li, Y. (2018) Effects of the sea floor topography on the 1D inversion of time-domain marine controlled source electromagnetic data. *Geophysical Prospecting*, 66(8), 1602–1624.

Cole, K.S. and Cole, R.H. (1941) Dispersion and absorption in dielectrics. I. alternating current characteristics. *The Journal of Chemical Physics*, 9(4), 341–351.

Commer, M. (2003) *Three-dimensional inversion of transient-electromagnetic data: a comparative study*. PhD thesis, University of Cologne.

Constable, S.C., Parker, R.L. and Constable, C.G. (1987) Occam's inversion: a practical algorithm for generating smooth models from electromagnetic sounding data. *Geophysics*, 52(3), 289–300.

Dill, H.G. (1993) Die Antimonvorkommen der mitteleuropäischen Alpiden und Variszisden. *Z Dtsch Geol Ges*, 144, 434–450.

Edwards, R.N. (1997) On the resource evaluation of marine gas hydrate deposits using sea-floor transient electric dipole–dipole methods. *Geophysics*, 62(1), 63–74.

Egbert, G.D. and Booker, J.R. (1986) Robust estimation of geomagnetic transfer functions. *Geophysical Journal of the Royal Astronomical Society*, 87(1), 173–194.

Gräbe, R., Schlegel, G. and Wiefel, H. (1996) *Digitale geologische Karte von Thüringen 1:25000, Blatt 5436 Schleiz*. Thüringer Landesanstalt für Umwelt und Geologie, Jena, Germany.

Grayver, A.V., Streich, R. and Ritter, O. (2013) Three-dimensional parallel distributed inversion of CSEM data using a direct forward solver. *Geophysical Journal International*, 193(3), 1432–1446.

Hanstein, T., Eilenz, H. and Strack, K. (1986) Einige Aspekte der Aufbereitung von LOTEM Daten. In: *Protokoll über das 11. Kolloquium Elektromagnetische Tiefenforschung*, pp. 319–328.

Haroon, A., Adrian, J., Bergers, R., Gurk, M., Tezkan, B., Mammadov, A. and Novruzov, A. (2015) Joint inversion of long-offset and central-loop transient electromagnetic data: application to a mud volcano exploration in Perekishkul, Azerbaijan. *Geophysical Prospecting*, 63(2), 478–494.

Hoheisel, A. (2000) *Untersuchung des Einflusses von Induzierter Polarisation (IP) auf Long-Offset Transient Electromagnetics (LOTEM)*. Master's thesis, University of Cologne, Institute for Geophysics and Meteorology.

Hoheisel, A., Hördt, A. and Hanstein, T. (2004) The influence of induced polarization on long-offset transient electromagnetic data. *Geophysical Prospecting*, 52(5), 417–426.

Hördt, A. (1989) *Ein Verfahren zur Joint Inversion angewandt auf Long Offset Electromagnetics (LOTEM) und Magnetotellurik (MT)*. Diploma thesis, University of Cologne.

Hördt, A. (1992) *Interpretation transient elektromagnetischer Tiefensondierungen für anisotrop horizontal geschichtete und für dreidimensionale Leitfähigkeitsstrukturen*. PhD thesis, University of Cologne.

Kaufman, A.A. and Keller, G.V. (1983) *Frequency and Transient Soundings*, Vol. 16. Elsevier.

Key, K. and Ovall, J. (2011) A parallel goal-oriented adaptive finite element method for 2.5-D electromagnetic modelling. *Geophysical Journal International*, 186(1), 137–154.

Kingman, J.E., Halverson, M. and Garner, S.J. (2004) *Stacking of controlled source electrical geophysical data*, Terrigena technical white paper number 20040328.0101(e), Available at: http://www.terngena.com/images/stones/pdf/Terrigena.0101%28e%29.Stacking.USLetter.pdf [Accessed 20 January 2015].

Levenberg, K. (1944) A method for the solution of certain non-linear problems in least squares. *Quarterly of applied mathematics*, 2(2), 164–168.

Liebe, K.T., Zimmermann, E., Kaiser, E. and Weise, E. (1912) *Digitale geologische Karte von Thüringen 1:25000, Blatt 5437 Mühltroff*. Thüringer Landesanstalt für Umwelt und Geologie, Jena, Germany.

Marquardt, D.W. (1963) An algorithm for least-squares estimation of nonlinear parameters. *Journal of the society for Industrial and Applied Mathematics*, 11(2), 431–441.

Martin, R. (2009) *Development and application of 2D and 3D transient electromagnetic inverse solutions based on adjoint Green functions: a feasibility study for the spatial reconstruction of conductivity distributions by means of sensitivities*. PhD thesis, University of Cologne.

Martin, T., Flores-Orozco, A., Guenther, T. and Dahlin, T. (2018) Comparison of TDIP and SIP measurements in the field scale. In: *5th International Workshop on Induced Polarization*, 3–5 October 2018, Newark, NJ.

Mörbe, W. (2020) *Deep controlled source electromagnetics for mineral exploration: a multidimensional validation study in time and frequency domain*. PhD thesis, University of Cologne.

Nabighian, M.N. and Elliot, C.L. (1976) Negative induced-polarization effects from layered media. *Geophysics*, 41(6), 1236–1255.

Nittinger, C., Cherevatova, M., Becken, M., Rochlitz, R., Günther, T., Martin, T. and Matzander, U. (2017) Novel semi-airborne CSEM system for the exploration of mineral resources. In: *EGU General Assembly Conference Abstracts*, Vol. 19, p. 15439.

Oldenburg, D.W., Haber, E. and Shekhtman, R. (2012) Three dimensional inversion of multisource time domain electromagnetic data. *Geophysics*, 78(1), E47–E57.

Pankratov, O.V. and Geraskin, A.I. (2010) On processing of controlled source electromagnetic (CSEM) data. *Geologica Acta*, 8(1), 0031–49.

Schiffler, M., Chwala, A., Kukowski, N., Meyer, H.G., Meyer, M., Meyer, U. and Stolz, R. (2017) Development of new magnetic field

sensors for electromagnetic mineral exploration in the DESMEX project. In *Frühjahrstagung der Deutschen Geophysikalischen Gesellschaft*.

Scholl, C. (2001) *Die Periodizität von Sendesignalen bei LOTEM*. Diploma thesis, University of Cologne.

Scholl, C. and Edwards, R.N. (2007) Marine downhole to seafloor dipole–dipole electromagnetic methods and the resolution of resistive targets. *Geophysics*, 72(2), WA39–WA49.

Smirnova, M.V., Becken, M., Nittinger, C., Yogeshwar, P., Mörbe, W., Rochlitz, R., Steuer, A., Costabel, S., Smirnov, M.Y. and Group, D.W. (2019) A novel semiairborne frequency-domain controlled-source electromagnetic system: three-dimensional inversion of semiairborne data from the flight experiment over an ancient mining area near Schleiz, Germany. *Geophysics*, 84(5), E281–E292.

Spagnoli, G., Hannington, M., Bairlein, K., Hördt, A., Jegen, M., Petersen, S. and Laurila, T. (2016) Electrical properties of seafloor massive sulfides. *Geo-Marine Letters*, 36(3), 235–245.

Spies, B.R. and Frischknecht, F.C. (1991) Electromagnetic sounding. *Electromagnetic Methods in Applied Geophysics*, 2(Part A), 285–426.

Steuer, A., Siemon, B., Pielawa, J., Petersen, H., Vob, V., Balzer, H.U. and Plath, C. (2015) *Zwischenbericht Hubschraubergeophysik Befliegung DESMEX Teil 1*. Technical report, Bundesanstalt für Geowissenschaften und Rohstoffe.

Strack, K.-M. (1992) *Exploration with Deep Transient Electromagnetics*, Vol. 30. Elsevier.

Streich, R. (2016) Controlled-source electromagnetic approaches for hydrocarbon exploration and monitoring on land. *Surveys in Geophysics*, 37(1), 47–80.

Yogeshwar, P., Küpper, M., Tezkan, B., Rath, V., Kiyan, D., Byrdina, S., Cruz, J. Andrade, C. and Viveiros, F. (2020) Innovative boat-towed transient electromagnetics—investigation of the Furnas volcanic lake hydrothermal system, Azores. *Geophysics*, 85(2), E41–E56.

Zhdanov, M.S. (2002) *Geophysical Inverse Theory and Regularization Problems*, Vol. 36. Elsevier.

Zhdanov, M.S. (2010) Electromagnetic geophysics: notes from the past and the road ahead. *Geophysics*, 75(5), 75A49–75A66.

Ziolkowski, A., Hobbs, B.A. and Wright, D. (2007) Multitransient electromagnetic demonstration survey in France. *Geophysics*, 72(4), F197–F209.